Case Studies in Thermal Engineering 42 (2023) 102709

Contents lists available at ScienceDirect

Case Studies in Thermal Engineering

journal homepage: www.elsevier.com/locate/csite

Galerkin computational work on thermally enhancement process in complex rheological generalized theory due to 3D-partially ionized rotational flow

Nattakan Boonsatit [a], Muhammad Sohail [b,*], Kanit Mukdasai [c], Umar Nazir [c], Manoj Singh [d], Abha Singh [e], Chandika Rama Mohan [f], Anuwat Jirawattanapanit [g], Ahmed M. Galal [h,i], Mohamed R. Ali [j,**]

[a] Faculty of Science and Technology, Rajamangala University of Technology Suvarnabhumi, Thailand
[b] Department of Mathematics, Khwaja Fareed University of Engineering & Information Technology, Rahim Yar Khan, 64200, Pakistan
[c] Department of Mathematics, Faculty of Science, Khon Kaen University, Khon Kaen, 40002, Thailand
[d] Department of Mathematics, Faculty of Science, Jazan University, Jazan, Saudi Arabia
[e] Department of Basic Sciences, College of Sciences and Theoretical Studies, Dammam-branch, Saudi Electronic University, Riyad, Saudi Arabia
[f] Clinical Nutrition Department Applied Medical Science College Jazan University, Saudi Arabia
[g] Department of Mathematics, Faculty of Science, Phuket Rajabhat University (PKRU), Thailand
[h] Mechanical Engineering Department, College of Engineering, Prince Sattam Bin Abdulaziz University, Wadi addawaser, 11991, Saudi Arabia
[i] Production Engineering and Mechanical Design Department, Faculty of Engineering, Mansoura University, P.O 35516, Mansoura, Egypt
[j] Faculty of Engineering and Technology, Future University, Cario, Egypt

ARTICLE INFO

Keywords:
3D-modeling
Power law model
Thermal enhancement
Partially flow
Non-Fourier's theory
Computational study

ABSTRACT

In this development, utilization of hybrid nanoparticles to investigate heat transfer enhancement in partially ionized liquid and generalized heat flux model. The phenomenon of momentum and thermal transport is discussed in a rotating frame and the features of hybrid nanoparticles have been monitored. The conservation laws are derived in Cartesian coordinates in a rotating frame for momentum and heat transfer laws. Current developing model is widely utilized dental products, automotive parts, electrical insulators, fuel cells, solar energy, optical chemical sensors, hair care products, engineering process, solar cells, green tires and electrical insulators etc. The concept of BL (boundary layer) is engaged to simplify the developing problem in terms of PD-equations. The derived PD-equations are changed into OD-equations by using transformations. Transformed problem is coupled nonlinear whereas the solution in terms of exactness does not exist. For the approximate solution, finite element procedure is chosen and the convergence has been shown through grid independent analysis. Several plots are developed to capture the contribution of several parameters to the solution. Velocity gradient (skin friction coefficient) declines with inclination in Hall currents, ion slip number but opposite trend was addressed against inclination of Lorentz force and power law index . It is recorded that for nonlinear problems a finite element scheme is a better tool.

* Corresponding author.
** Corresponding author.
E-mail addresses: muhammad_sohail111@yahoo.com (M. Sohail), mohamed.reda@fue.edu.eg (M.R. Ali).

https://doi.org/10.1016/j.csite.2023.102709
Received 4 December 2022; Received in revised form 21 December 2022; Accepted 4 January 2023
Available online 7 January 2023

Nomenclature:

W, U, V	Velocity components (ms^{-1})
K_1	Consistency coefficient
ω	Rotating velocity (ms^{-1})
G	Gravitational acceleration (ms^{-2})
σ	Electrical conductivity (Sm^{-1})
T_∞, T	Ambient temperature and temperature (K)
C_p	Specific heat capacity (ms^{-1})
λ_1	Thermal relaxation number
a	Stretching number along x-axis
ε_1	Temperature dependent parameter
ODEs	Ordinary differential equations
C_g, C_f	Skin friction coefficients
Nu	Nussselt number
τ_{ij}	Stress tensor
D_{ij}	Stream rate tensor
y, x, z	Space coordinates (m)
m	Power law index number
ρ	Fluidic density (Kgm^{-3})
β_2, β_1	Coefficients of thermal expansion
B_0	Magnetic induction $(NsC^{-1}m^{-1})$
β_e, β_i	Ion slip and Hall parameters
k	Thermal conductivity (Wm^{-1})
T_w	Wall temperature (K)
∞	Infinity
φ_1, φ_2	Volume fractions of nanoparticles
BCs	Boundary conditions
Re	Reynolds number
ν	Kinematic viscosity (m^2s^{-1})
w_1, w_3, w_2	Weight functions
τ_{yz}, τ_{xz}	Stress tensors

1. Introduction

Thermal features are an interesting field of research due to their wider applications. Influence of nanoparticles is essential to increase the thermal transport. So far, an extensive research work has been carried out on nanoparticles having applications utilized in applied science and engineering processes. For instance, Nazir et al. [1] investigated comparing thermal features among hybrid nanomaterial and tri-hybrid nanomaterial in the rheology of Sisko martial involving thermal properties. Sohail et al. [2] modeled numerical aspects of viscoelastic fluid in heat energy phenomena involving variable thermal properties. Nazir et al. [3] discussed thermal features of Prandtl liquid including non-Fourier's under action of variable thermal characteristics over a surface. Nazir et al. [4] used an exact solution approach to visualize thermal aspects of Casson liquid past the stretchable surface. Sohail et al. [5] derived consequences of Casson liquid involving Joule heating as well as viscous dissipation using 3D surface. Waqas et al. [6] bio-convective flow of modified viscoelastic second grade and handled the complex equations numerically. They found that higher values of Peckelt number reduce the density profile of microorganisms. Nazir et al. [7] investigated thermal performance of tri-hybrid nanomaterial in Sisko martial involving variable thermal properties. They implemented a numerical approach to obtain numerical results. Algehyne et al. [8] examined the effects of thermal transport on a pseudo-plastic material by heating and stretching a porous sheet. To stimulate energy conservation, heat generation and absorption are used. Prandtl's boundary-layer approach was used to model the phenomenon in Cartesian coordinates to make the problem easier to understand. The rheology is modeled using nonlinear coupled PDEs. Similarity transformation is used to convert these derived PDEs to ODEs. The converted ODEs with their new parameters were numerically approximated using the finite element method. In this study's limiting case, it was discovered that the obtained solution was consistent with previously published findings. FEM is an excellent approach for solving nonlinear problems in mathematical modeling, among other things. Hafeez et al. [9] created it to use a system of PDEs to simulate the thermal and solute properties of the Casson liquid in a Darcy porous medium. Convective boundary conditions determine how models behave in these situations. Mahbood [10] developed a system for performing his calculations. MHD couple stress fluid was studied in greater depth employing a numerical approach. Mahbood [11] investigated the heat and mass transfer properties of a Brinkmann-type nanofluid flow composed of sodium alginate and Fe_3O_4 in a vertical rotating frame. The Runge-Kutta Fehlberg method (RKF-45) solves dimensionless nonlinear partial differential

Table 1
Thermal properties for MoS_2 and SiO_2 in base liquid [36].

ρ	C_p	k	σ
$C_2H_6O_2(=\mathbf{1113.5})$	$C_2H_6O_2(=\mathbf{1113.5})$	$C_2H_6O_2(=\mathbf{0.253})$	$C_2H_6O_2(=\mathbf{4.3}\times\mathbf{10^{-5}})$
$MoS_2(=\mathbf{2650})$	$MoS_2(=\mathbf{2650})$	$MoS_2(=\mathbf{1.5})$	$MoS_2(=\mathbf{0.0005})$
MoS_2 and $SiO_2(=\mathbf{5060})$	MoS_2 and $SiO_2(=\mathbf{5060})$	MoS_2 and $SiO_2(=\mathbf{34.5})$	MoS_2 and $SiO_2(=\mathbf{1}\times\mathbf{10^{-18}})$

equations. Ayub [12] investigated the second-order slip phenomenon and the flow of cross nanofluids that comes to a halt at a certain point using a spectral relaxation method. Brownian motion, joules, viscous heating, thermophoresis, and mixed convection are all considered. The way MHD transferred heat was studied by Shah's [13] interest. The velocity and activation energy of nanofluid are determined using perpendicular magnetic dipole field measurements. Ezaier et al. [14] discussed the morphological properties associated with interfaces growth in composite membranes. Ezaier et al. [15] estimated performance of diffusion retention in composite membranes. Hamad et al. [16] investigated dynamics consequences of nanofluid in viscoelastic fluid considering thermal radiation and Lorentz force containing gyrotactic microorganisms over a stretching surface. Algehyne et al. [17] discussed influences of Lorentz forces in Buongiorno's fluid model considering multiple effects involving alumina-water nanofluid in slippery curved geometry. Rasool et al. [18] performed EMHD nanofluid considering Darcy-Forchheimera approach in a heated Riga plate using generalized transfer laws. Wakif et al. [19] discussed new insights regarding ethylene glycol using Buongiorno's approach past a stretching surface. Studies related to nanofluid in non-Newtonian and Newtonian fluids considering multiple effects over stretching surface are revealed in Refs. [20–28]. Reddy et al. [29] discussed consequences of buoyant flow in hybrid nanofluid considering heated annulus via non-uniformly. Sankar et al. [30] investigated impacts of non-uniform heating phenomena in nanofluid-filled annulus. Balasundaram et al. [31] estimated hydrocephalic cerebrospinal for rotational flow of fluid within pulsatile boundaries. Dharmaiah et al. [32] discussed thermal aspects in tangent hyperbolic fluid utilizing nanoparticles along with activation energy under thermal radiations. Vedavathi et al. [33] studied mass diffusion and heat characterizations of hyperbolic tangent liquid in hyperbolic tangent liquid in the presence of chemical species via applications of engineering. Several important aspects are recorded in Refs. [37–40] and the studies mentioned therein.

Existing literature reveals that study related to 3D power law model is studied in the presence of generalized theory past a 3-dimensional vertical rotating stretching frame or plate. Further, correlations regarding hybrid and nano-fluid are added. Constant magnetic field is attached at walls to study configurations of Lorentz force on flow and thermal energy. Such a complex model is numerically handled by a finite element method. Basically, current analysis is divided into five sections which are introduction, mathematical procedure, numerical method, explanation of results and conclusion, respectively.

2. Mathematical procedure

Consider a 3D-power law model developed under the occurrence of partial flow past a vertical surface. The acceleration into hybrid nanoparticles is induced using movement of the wall along horizontal direction. Further, a constant magnetic region is used in vertical

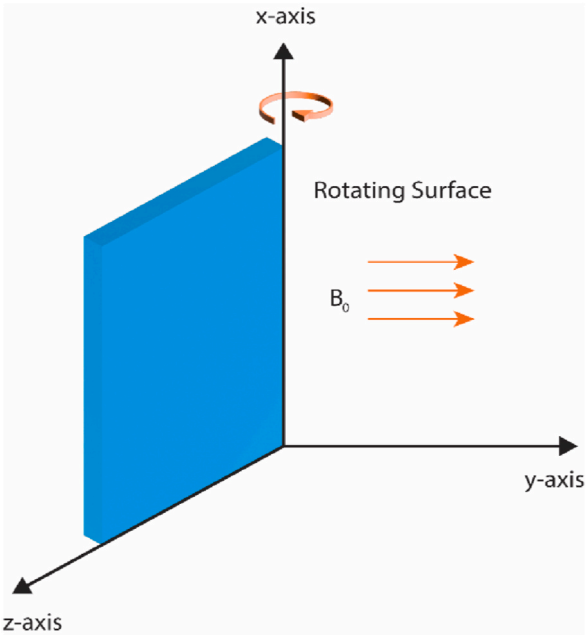

Fig. 1. Physical diagram of current model.

direction. CCM (Cattaneo-Christov model) is considered in the presence of thermal energy dependent thermal conductivity. The velocities of the wall produce the motion into fluidic particles. Properties based on thermal characteristics are mentioned in Table 1. Flow configuration is carried out by Fig. 1. PDEs are reduced using the concept of BLAs (boundary layer analysis). Fig. 1 shows the geometrical trend of the developed model.

Stress tensor of Power law model is defined [34] as

$$\tau_{ij} = 2K_1\left[2D_{Kl}D_{Kl}\right]^{\frac{n-1}{2}}D_{ij}, D_{ij} = \left(\frac{\partial U_i}{\partial x_j} + \frac{\partial U_j}{\partial x_i}\right). \tag{1}$$

Using BLAs (boundary layer approximations) on Eq. (1) and Eq. (1) is reduced as

$$\tau_{yz} = K_1\left|\frac{\partial U}{\partial z}\right|^{n-1}\frac{\partial V}{\partial z}, \tau_{xz} = K_1\left|\frac{\partial U}{\partial z}\right|^{n-1}\frac{\partial U}{\partial z}. \tag{2}$$

Hence, PDEs [34,35] are

$$\frac{\partial U}{\partial x} + \frac{\partial V}{\partial y} + \frac{\partial W}{\partial z} = 0, \tag{3}$$

$$U\frac{\partial U}{\partial x} + V\frac{\partial U}{\partial y} + W\frac{\partial U}{\partial z} = 2\omega v + \frac{K_1}{\rho_{hnf}}\frac{\partial}{\partial Z}\left(\left|\frac{\partial U}{\partial z}\right|^{n-1}\frac{\partial U}{\partial z}\right) + G\beta_1(T - T_\infty) + \frac{\sigma_{hnf}(B_0)^2}{\rho_{hnf}\left[(\beta_e)^2 + (1+\beta_e\beta_i)^2\right]}[\beta_e V - (1+\beta_e\beta_i)U], \tag{4}$$

$$U\frac{\partial V}{\partial x} + V\frac{\partial V}{\partial y} + W\frac{\partial V}{\partial z} = -2\omega u + \frac{K_1}{\rho_{hnf}}\frac{\partial}{\partial Z}\left(\left|\frac{\partial U}{\partial z}\right|^{n-1}\frac{\partial V}{\partial z}\right) - \frac{\sigma_{hnf}(B_0)^2}{\rho_{hnf}\left[(\beta_e)^2 + (1+\beta_e\beta_i)^2\right]}[\beta_e U + (1+\beta_e\beta_i)V] + G\beta_2(T - T_\infty), \tag{5}$$

$$\begin{aligned} U\frac{\partial T}{\partial x} + V\frac{\partial T}{\partial y} + W\frac{\partial T}{\partial z} &= \frac{1}{(\rho C_p)_{hnf}}\frac{\partial}{\partial y}\left(k_{hnf}\frac{\partial T}{\partial y} + k_{hnf}\frac{\partial T}{\partial x} + k_{hnf}\frac{\partial T}{\partial z}\right)\lambda_1\left(U^2\frac{\partial^2 T}{\partial x^2} + V^2\frac{\partial^2 T}{\partial y^2} + W^2\frac{\partial^2 T}{\partial y^2}\right) \\ &+ \lambda_1\left(U\frac{\partial U}{\partial x} + V\frac{\partial U}{\partial y} + W\frac{\partial U}{\partial z}\right)\frac{\partial T}{\partial x}\,2\lambda_1\left(UV\frac{\partial^2 T}{\partial x\partial z} + WV\frac{\partial^2 T}{\partial y\partial z} + UW\frac{\partial^2 T}{\partial x\partial z}\right) + \lambda_1\left(U\frac{\partial V}{\partial x} + V\frac{\partial V}{\partial y} + W\frac{\partial V}{\partial z}\right)\frac{\partial T}{\partial y} \\ &+ \lambda_1\left(U\frac{\partial W}{\partial x} + V\frac{\partial W}{\partial y} + W\frac{\partial W}{\partial z}\right)\frac{\partial T}{\partial z}. \end{aligned} \tag{6}$$

The required boundary conditions [34,35] are mentiioned as

$$U = a(x+y), T = T_w, V = a(x+y), w = 0 \text{ at } z = 0, T \to T_\infty, V \to 0, U \to 0, \text{when } z \to \infty. \tag{7}$$

Variables transformations [34] are

$$U = a(x+y)F', V = a(x+y)G, \theta = \frac{T - T_\infty}{T_w - T_\infty}, k_{hnf} = k_{hnf}\left[1 + \varepsilon_1\left(\frac{T - T_\infty}{T_w - T_\infty}\right)\right],$$

$$\eta = \left(\frac{ba^{n-2}}{\rho_f}\right)^{\frac{1}{n+1}} z x^{\frac{1-n}{1+n}}, W = -a\left(\frac{ba^{n-2}}{\rho_f}\right)^{\frac{1}{n+1}}\left[\frac{2n}{n+1}F + \frac{1-n}{1+n}\eta F' + G\right](x+y)^{\frac{1-n}{1+n}}. \tag{8}$$

Thermal correlations [36] for mono and hybrid fluids are

$$\left.\begin{aligned} \rho_{hnf} &= \left[(1-\varphi_2)\left\{(1-\varphi_1)\rho_f + \varphi_1\rho_{s1}\right\}\right] + \varphi_2\rho_{s2} \\ \left(\rho C_p\right)_{hnf} &= \left[(1-\varphi_2)\left\{\begin{matrix}(1-\varphi_1)\left(\rho C_p\right)_f \\ +\varphi_1\left(\rho C_p\right)_{s1}\end{matrix}\right\}\right] + \varphi_1\left(\rho C_p\right)_{s2} \\ \left\{\frac{k_{s1} + (n-1)k_f - (n-1)\varphi_1\left(k_f - k_{s2}\right)}{k_{s1} + (n-1)k_f - \varphi_1\left(k_{s2} - k_f\right)}\right\} &= \frac{k_{bf}}{k_f} \end{aligned}\right\}, \tag{9}$$

$$\left.\begin{aligned} \mu_{hnf} &= \frac{(1-\varphi_2)^{2.5}\mu_f}{(1-\varphi_1)^{2.5}}, \frac{k_{nf}}{k_f} = \left\{\frac{k_s + (n+1)k_f - (n-1)\varphi\left(k_f - k_s\right)}{k_s + (n-1)k_f + \varphi\left(k_f - k_s\right)}\right\} \\ \frac{k_{hnf}}{k_{bf}} &= \left\{\frac{k_{s2} + (n-1)k_{bf} - (1-n)\varphi_2\left(k_{s2} - k_{bf}\right)}{k_{s2} + (n-1)k_{bf} - \varphi_2\left(k_{bf} - k_{s2}\right)}\right\} \\ \left\{\frac{k_{s2} + (n-1)k_{bf} - (1-n)\varphi_2\left(k_{s2} - k_{bf}\right)}{k_{s2} + (n-1)k_{bf} - \varphi_2\left(k_{bf} - k_{s2}\right)}\right\} &= \frac{k_{hnf}}{k_{bf}} \end{aligned}\right\}, \tag{10}$$

$$\frac{k_{hnf}}{k_{bf}}=\left\{\begin{array}{l}\left\{\begin{array}{l}\dfrac{\frac{k_{s2}}{k_{bf}}+\omega+\omega\varphi_2\left(1-\frac{k_{s2}}{k_{bf}}\right)}{\frac{k_{s2}}{k_{bf}}+\omega+\varphi_2\left(1-\frac{k_{s2}}{k_{bf}}\right)}\end{array}\right\}\omega=2\varphi_2{}^{\frac{1}{5}}\dfrac{L}{D}\text{ for cylindrical particle}\\ \omega=2\varphi_2{}^{1/5}\text{ for spherical particle}\end{array}\right\},\tag{11}$$

$$\frac{k_{hnf}}{k_{bf}}=\left\{\begin{array}{l}\left\{\begin{array}{l}\dfrac{\frac{k_{s1}}{k_f}+\omega+\omega\varphi_1\left(1-\frac{k_{s1}}{k_f}\right)}{\frac{k_{s1}}{k_f}+\omega+\varphi_1\left(1-\frac{k_{s1}}{k_f}\right)}\end{array}\right\}\omega=2\varphi_2{}^{\frac{1}{5}}\dfrac{L}{D}\text{ for cylindrical particle}\\ \omega=2\varphi_2{}^{1/5}\text{for spherical particles}\end{array}\right\}.\tag{12}$$

Dimensionless form regarding ODEs [34,35] is formulated as

$$\left(|F''|^{n-1}F''\right)'-\frac{\nu_{hnf}}{\nu_f}\left[(F')^2\right]+\frac{M^2}{(\beta_e)^2+(1+\beta_e\beta_i)^2}\left[\beta_eG-(1+\beta_e\beta_i)F'\right]-\frac{\nu_{hnf}}{\nu_f}\left(\frac{2n}{n+1}F+G\right)F''+\frac{\nu_f}{\nu_{hnf}}2G\Omega=0,\tag{13}$$

$$\left(|F'|^{n-1}G'\right)'-\frac{\nu_{hnf}}{\nu_f}(G)^2-\frac{M^2}{(\beta_e)^2+(1+\beta_e\beta_i)^2}\left[\beta_eF'+(1+\beta_e\beta_i)G\right]-\frac{\nu_{hnf}}{\nu_f}\left(\frac{2n}{n+1}F+G\right)G'-2\frac{\nu_f}{\nu_{hnf}}F'\Omega=0,\tag{14}$$

$$(1+\varepsilon_1\Theta)\Theta''+\frac{(\rho C_p)_{hnf}k_f}{(\rho C_p)_fk_{hnf}}\left[\left(\frac{2n}{1+n}\right)PrF\Theta'+PrG\Theta'\right]-\frac{(\rho C_p)_{hnf}k_f}{(\rho C_p)_fk_{hnf}}Pr\lambda_a\left[\left(\frac{2n}{1+n}F+G\right)\left(\frac{2n}{1+n}F'+G\right)\Theta'+\left(\frac{2n}{1+n}F+G\right)^2\Theta''\right]=0.\tag{15}$$

Dimensionless parameters are derived as

$$Re=\frac{x^n\rho_f(U_w)^{2-n}}{k_f},M^2=\frac{2B_0^2\sigma_f}{\rho_fa},\Omega=\frac{\omega}{a},\lambda_a=\frac{\lambda_1a}{x},Pr=\frac{(C_p)_fax^2Re^{\frac{2}{n+1}}}{k_f}.$$

Dimensionless B-conditions are

$$G(\infty)=0,F'(\infty)=0,\theta(0)=1,F'(0)=1,\theta(\infty)=0,G(0)=0,F(0)=0.\tag{16}$$

Skin friction coefficients [35] in vertical and horizontal directions is prescribed as

$$C_{fx}=\frac{\tau_{zy}|_{z=0}}{\rho_f(U_w)^2},(Re)^{\frac{1}{n+1}}C_g=\frac{1}{(1-\varphi_2)^{2.5}(1-\varphi_1)^{2.5}}|F''(0)G'(0)|^n,\tag{17}$$

$$C_{fy}=\frac{\tau_{zx}|_{z=0}}{\rho_f(U_w)^2},(Re)^{\frac{1}{n+1}}C_f=\frac{1}{(1-\varphi_2)^{2.5}(1-\varphi_1)^{2.5}}|F''(0)|^n.\tag{18}$$

Nusselt number [35] is delivered as

$$Nu=\frac{q_wx}{(T_w-T_\infty)k_f},q_w=-k_{hnf}\frac{\partial T}{\partial z}|_{z=0},Nu(Re)^{\frac{-1}{n+1}}=\frac{k_{hnf}}{k_f}\Theta'(0).\tag{19),(20}$$

3. Finite element method

A system of dimensionless non-linear ODEs is tackled with help of finite element method (FEM) [36]. Eqs. 13–15 are numerically handled by finite element analysis. Governing equations in view of ODEs are known as residual forms. Residuals form equations are changed into weak form. Galerkin approximations are utilized to estimate weak forms inserting linear type shape functions. Development of stiffness matrices are derived over elements. Analysis of the assembly process is implemented for derivation of algebraic equations and these equations are changed into linear equations using Picard linearization scheme. Process regarding iteration of equations is solved. Compute code (FEM) is developed on MAPLE 18 and accuracy of code is verified with already published work [34]. The procedure regarding computational is discussed below.

Obtained residuals of current OD-equations are

$$\int_{\eta_e}^{\eta_{e+1}}w_1(F'-H)d\eta=0,\tag{21}$$

$$\int_{\eta_e}^{\eta_{e+1}} w_2 \left[\begin{array}{l} \left(|H^{'}|^{n-1}H^{'}\right)^{'} - \frac{\nu_{hnf}}{\nu_f}\left[(F^{'})^2\right] - \frac{\nu_{hnf}}{\nu_f}\left(\frac{2n}{n+1}F+G\right)H^{'} \\ +\frac{M^2}{(\beta_e)^2+(1+\beta_e\beta_i)^2}\{\beta_e G-(1+\beta_e\beta_i)H\} + \frac{\nu_f}{\nu_{hnf}}2G\Omega \end{array} \right] d\eta = 0, \tag{22}$$

$$\int_{\eta_e}^{\eta_{e+1}} w_3 \left[\begin{array}{l} \left(|F^{'}|^{n-1}G^{'}\right)^{'} - \frac{\nu_{hnf}}{\nu_f}(G)^2 - \frac{\nu_{hnf}}{\nu_f}\left(\frac{2n}{n+1}F+G\right)G^{'} \\ -2\frac{\nu_f}{\nu_{hnf}}H\Omega - \frac{M^2}{(\beta_e)^2+(1+\beta_e\beta_i)^2}\{\beta_e H+(1+\beta_e\beta_i)G\} \end{array} \right] d\eta = 0, \tag{23}$$

$$\int_{\eta_e}^{\eta_{e+1}} w_4 \left[\begin{array}{c} (1+\varepsilon_1\Theta)\Theta'' + \frac{(\rho C_p)_{hnf}k_f}{(\rho C_p)_f k_{hnf}}\left\{\left(\frac{2n}{1+n}\right)PrF\Theta^{'}+PrG\Theta^{'}\right\} \\ -\frac{(\rho C_p)_{hnf}k_f}{(\rho C_p)_f k_{hnf}}Pr\,\lambda_a\left\{\left(\frac{2n}{1+n}F+G\right)\left(\frac{2n}{1+n}H+G\right)\Theta^{'}\right\} \\ -\frac{(\rho C_p)_{hnf}k_f}{(\rho C_p)_f k_{hnf}}Pr\,\lambda_a\left(\frac{2n}{1+n}F+G\right)^2\Theta'' \end{array} \right] d\eta = 0, \tag{24}$$

Desired stiffness matrices are derived as

$$K_{ij}^{14}=0, K_{ij}^{11}=\int_{\eta_e}^{\eta_{e+1}}\left(\frac{d\psi_j}{d\eta}\psi_i\right)d\eta, K_{ij}^{12}=-\int_{\eta_e}^{\eta_{e+1}}\left(\psi_j\psi_i\right)d\eta, K_{ij}^{13}=0, \tag{25}$$

$$K_{ij}^{22}=\int_{\eta_e}^{\eta_{e+1}}\left[\begin{array}{c} -(n-1)(\overline{H}^{'})^{n-2}\frac{d\psi_i}{d\eta}\frac{d\psi_j}{d\eta}+\frac{M^2}{(\beta_e)^2+(1+\beta_e\beta_i)^2}\beta_e\psi_i\frac{d\psi_j}{d\eta} \\ -\frac{M^2}{(\beta_e)^2+(1+\beta_e\beta_i)^2}(1+\beta_e\beta_i)\psi_i\psi_j-\frac{\nu_{Thnf}}{\nu_f}\overline{H}\psi_i\psi_j \\ -\frac{\nu_{Thnf}}{\nu_f}\left(\frac{2n}{n+1}\overline{F}+\overline{G}\right)\psi_i\frac{d\psi_j}{d\eta} \end{array} \right] d\eta, \tag{26}$$

$$K_{ij}^{24}=0, K_{ij}^{23}=\int_{\eta_e}^{\eta_{e+1}}\frac{\nu_f}{\nu_{Th}}2\Omega\left(\psi_j\psi_i\right)d\eta, B_i^1=0, B_i^2=0, B_i^3=0, \tag{27}$$

$$K_{ij}^{33}=\int_{\eta_e}^{\eta_{e+1}}\left[\begin{array}{l} -(n-1)(\overline{H}^{'})^{n-2}\frac{d\psi_i}{d\eta}\frac{d\psi_j}{d\eta}-\frac{\nu_{Thnf}}{\nu_f}\overline{G}^{'}\psi_i\frac{d\psi_j}{d\eta}-\frac{M^2\beta_e\psi_i\psi_j}{(\beta_e)^2+(1+\beta_e\beta_i)^2} \\ -\frac{\nu_{Thnf}}{\nu_f}\overline{G}\frac{d\psi_i}{d\eta}\frac{d\psi_j}{d\eta}-\frac{\nu_{Thnf}}{\nu_f}\frac{2n\overline{F}}{n+1}\frac{d\psi_i}{d\eta}\frac{d\psi_j}{d\eta}-\frac{(1+\beta_e\beta_i)M^2\psi_i\psi_j}{(\beta_e)^2+(1+\beta_e\beta_i)^2} \end{array} \right] d\eta, \tag{28}$$

$$K_{ij}^{32}=\int_{\eta_e}^{\eta_{e+1}}\frac{\nu_f}{\nu_{Th}}2\Omega\left(\psi_j\psi_i\right)d\eta, K_{ij}^{31}=0, K_{ij}^{34}=0, B_i^3=0, \tag{29}$$

$$K_{ij}^{44}=\int_{\eta_e}^{\eta_{e+1}}\left[\begin{array}{c} -(1+\varepsilon_1\overline{\Theta})\frac{d\psi_i}{d\eta}\frac{d\psi_j}{d\eta}-\left(\frac{2n}{1+n}\overline{F}+\overline{G}\right)^2\frac{d\psi_i}{d\eta}\frac{d\psi_j}{d\eta} \\ +\frac{(\rho C_p)_{Thnf}k_f}{(\rho C_p)_f k_{Thnf}}\frac{2n}{1+n}Pr\overline{F}\psi_i\frac{d\psi_j}{d\eta}+\frac{(\rho C_p)_{Thnf}k_f}{(\rho C_p)_f k_{Thnf}}Pr\overline{G}\psi_i\psi_j \\ -\frac{(\rho C_p)_{Thnf}k_f}{(\rho C_p)_f k_{Thnf}}Pr\,\lambda_a\left(\frac{2n}{1+n}\overline{F}+\overline{G}\right)\left(\frac{2n}{1+n}\overline{H}+\overline{H}^{'}\right)\psi_i\frac{d\psi_j}{d\eta} \end{array} \right] d\eta. \tag{30}$$

An error analysis is delivered as

$$Err=\left|\Omega^{i-1}-\Omega^{i}\right|, \tag{31}$$

and criteria for error analysis is defined as

$$max\left|\Omega^{i-1}-\Omega^{i}\right|<10^{-8}. \tag{32}$$

It is noticed that MAPLE 18 is utilized to generate code of FEM. The solution of algebraic equations is simulated carried out by 300

elements and grid independent survey is presented in Table 3. Table 3 reveals comparative study for temperature gradient with published work and comparative investigation is listed in Table 2.

4. Discussion and results

Comparative thermal features among two kinds of hybrid nanofluid models with YO (Yamada Ota) and HC (Hamilton Crosser) models in power law fluid are visualized past the 3D vertical frame. It is noticed that suspension of nanoparticles named as aluminum oxide and silicon oxide in ethylene glycol are addressed. Ion slip, non-Fourier's and Hall forces are considered involving heat absorption/heat generation. Such considerations are addressed to develop a complex model which is simulated using a finite element approach. Graphical results regarding temperature and velocity are discussed below.

4.1. Features of parameters on velocity profile

Fig. 2a, b, 3a, 3b, 4a, 4b and 5a, 5b are plotted for velocity distribution versus several parameters (Ω, β_e, n and β_e). Impact of Ω on velocity curves is noticed on Fig. 2a and b. It is experienced that occurrence of Ω is modeled via rotating surface. Flow becomes gradually slow down when sheet is started rotate. Further, Behavior of fluid becomes thinning when Ω is enhanced. Therefore, motion is reduced against growing values of Ω. An increasing role of Ω on velocity region is noticed from Fig. 2a and b. Comparative flow features are measured among YO- and HC-models in term of hybrid nanofluid. The parameter related to Ω is dimensionless parameter and appearance of Ω is generated using rotational motion into particles. Frictional force is generated into particles due to rotational flow. Therefore, less acceleration (for both directions) is produced using enhancement in Ω. Motion for $\Omega = 0$ is higher than motion for $\Omega \neq 0$. Thickness and width for momentum layers can be distributed utilizing change in Ω. Fig. 3a, b, 4a and 4b are addressed to sketch estimation of Hall parameter and ion slip number on velocity distribution. It is included that acceleration into fluidic particles is inclined versus β_e and β_i. Generalized Ohm's theory is used in current analysis which is reason for development of β_e and β_i. Flow is enhanced because directly relation is observed among partially ionized particles and velocity distribution. Moreover, thickness in term of momentum boundary layers is inclined when Hall parameter and ion slip number are inclined. Performance of flow behavior for YO-model is greater than flow performance of HC-hybrid model. Flow distribution in y- and x-directions is performed against distribution in bouncy parameter. The occurrence of β_i and β_e in momentum is occurred due to Generalized Ohm's law. It is noticed that appearance of β_i and β_e is against applied magnetic field. Because magnetic field is occurred due to role of Lorentz force in fluidic particles and Lorentz force are opposite to β_e and β_i. Lorentz force is enhanced when β_i and β_e are increased. Therefore, Flow is enhanced versus β_i and β_e. The occurrence regarding β_i and β_e are occurred in denominator of Lorentz force. Alternatively, an inverse proportional relationship was observed among Lorentz force and Hall currents. Lorentz force enhances within different values for β_i and β_e. Hence, effects of β_i and β_e are estimated as favorable for obtaining maximum motion into particles. Physically, an inclination in β_i and β_e corresponds collisions among ionizations and electronic particles. Rate regarding collision is based on impacts of β_i and β_e. Therefore, a remarkable declination is studied in magnetic force within increasing values of β_i and β_e. Hence Role of n on flow distribution is addressed by Fig. 5a and b. Declination into motion related to fluidic particles is estimated against distribution in power law index parameter. It is captured that appearance of n is occurred considering concept of power law model in momentum equations. Further, inverse relation of thermal energy is noticed is noticed versus positive values of n. Therefore, a decreasing function of velocity profile is noticed when n is enhanced. Appearance of n is revealed as shear thinning behavior. It is observed that acceleration into fluidic particles is declined when power law index number is increased. Characterizations of fluids is based numerical values of n. Current problem becomes Newtonian fluid for $n = 1$ and behavior of fluid is treated as a pseudo-plastic for $n < 1$ while flow is known as a dilatant fluid for $n > 1$. Flow for $n = 1$ is greater than flow for $n > 1$. Thickness in view of momentum layers is magnified against change in n. Consequently, inverse proportional relation was addressed within numerical values of n.

4.2. Features of parameters on temperature profile

In this subsection, Fig. 6a, b and 6c are developed to estimate variation in heat energy characterizations versus the change in temperature dependent parameter, time relaxation number and n in the presence of two hybrid models. Fig. 6a is generated to measure estimation among thermal profile and (n). It is experienced that thermal transport among nanoparticles is decreased when n is enhanced. Moreover, thickness related to thermal energy is also decreasing function versus change in n. It is noticed that appearance of n is occurred using concept of power law fluidic model in momentum equations. Further, inverse relation of thermal energy is noticed versus positive values of n. Therefore, a decline function of thermal profile is noticed when n is enhanced. Characterizations of fluidic particles are based on numerical values of n. Behavior of fluid is known as a Newtonian fluid for $n = 1$. Temperature profile for $n = 1$ is greater than temperature profile for $n \neq 1$. Here dilatant fluid is studied in presence of multiple aspects for $n > 1$. Thermal thickness for generating layers is declined for dilatant fluid in current analysis. Appearance of n is revealed as shear thinning behavior. Fig. 6b is

Table 2
Validation results of present work with published study considering $\varphi_1 = 0.004, \varphi_2 = 0.0075, M = 0.001, Pr = 204, \beta_i = \beta_e = 0, \Omega = 0.1, \epsilon_1 = 0.0$.

	Adil Sadiq [34]	present work
n	$\frac{-1}{-Nu(Re)^{\frac{n+1}{n}}}$	$\frac{-1}{-Nu(Re)^{\frac{n+1}{n}}}$
1	3.40917113	3.4609170715
2	3.40830920	3.4087202243
3	3.74498557	3.7442430383

Table 3
The study related to mesh free analysis in view of temperature profile and velocity curves when $n = 1, M = 0.001, \beta_e = 0.2, \beta_i = 0.2, \Omega = 0.1, \varepsilon_1 = 0.3, Pr = 206, \lambda_a = 0.1, \varphi_1 = 0.004, \varphi_2 = 0.075$.

Number of elements	$F'\left(\frac{\eta_{max}}{2}\right)$	$G\left(\frac{\eta_{max}}{2}\right)$	$\theta\left(\frac{\eta_{max}}{2}\right)$
30	0.6586386817	0.0001721355025	0.6605821625
60	0.6233792179	0.0002229082388	0.6437292447
90	0.6116725178	0.0002319259575	0.6380761926
120	0.6058311283	0.0002348216628	0.6352430888
150	0.6023296966	0.0002360353595	0.6335412345
180	0.5999974251	0.0002366270036	0.6324058465
210	0.5983324921	0.0002369433746	0.6315945612
240	0.5970846646	0.0002371243282	0.6309857193
270	0.5961135026	0.0002372274024	0.6305118421
300	0.5953382626	0.0002400319135	0.6301326200

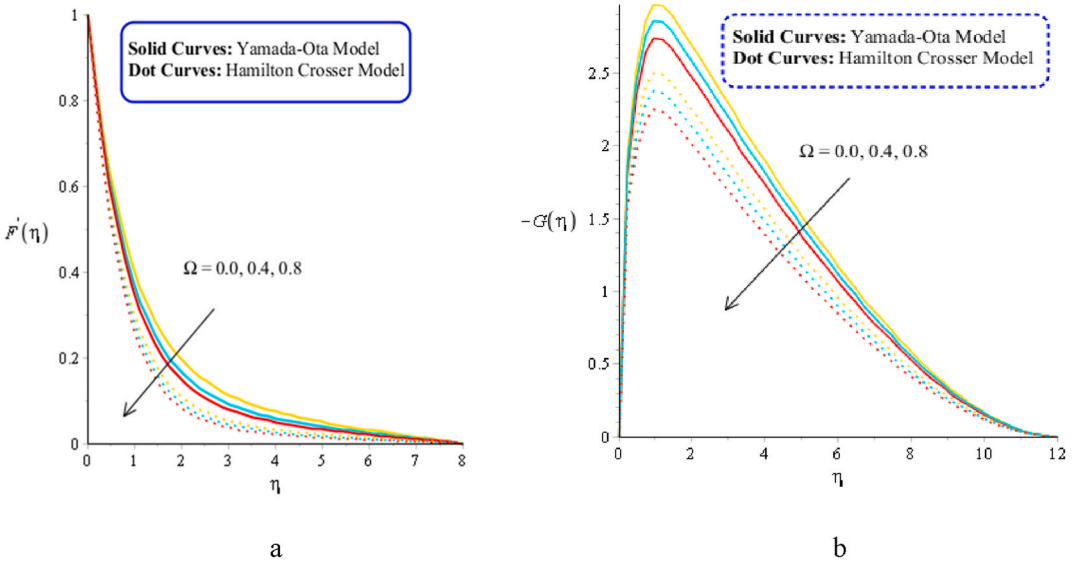

Fig. 2. Different values of Ω on $F'(\eta)$ and $G(\eta)$ when $n = 1, M = 0.003, \beta_e = 0.3, \beta_i = 0.2, \varepsilon_1 = 0.3, Pr = 208, \lambda_a = 0.4, \varphi_1 = 0.004, \varphi_2 = 0.075$.

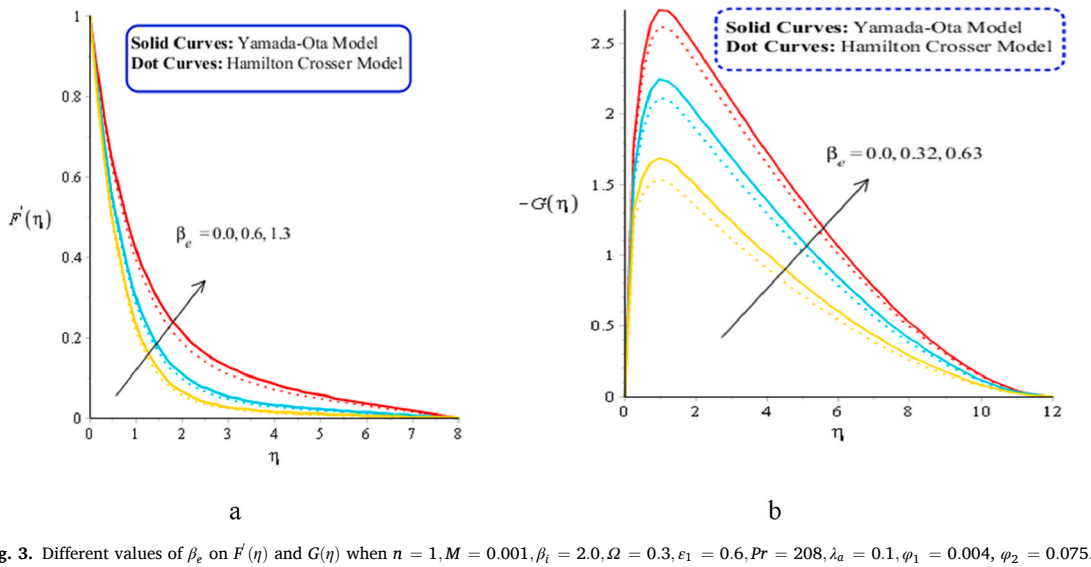

Fig. 3. Different values of β_e on $F'(\eta)$ and $G(\eta)$ when $n = 1, M = 0.001, \beta_i = 2.0, \Omega = 0.3, \varepsilon_1 = 0.6, Pr = 208, \lambda_a = 0.1, \varphi_1 = 0.004, \varphi_2 = 0.075$.

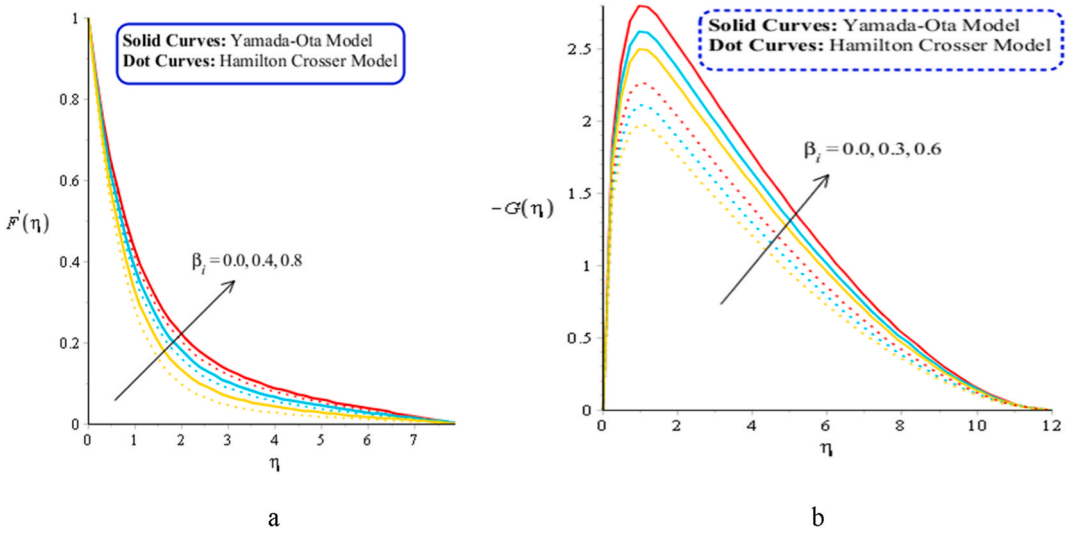

Fig. 4. Different values of β_i on $F'(\eta)$ and $G(\eta)$ when $n = 1, M = 0.005, \beta_e = 0.4, \Omega = 0.7, \varepsilon_1 = 2.3, Pr = 206, \lambda_a = 0.6, \varphi_1 = 0.004, \varphi_2 = 0.075$.

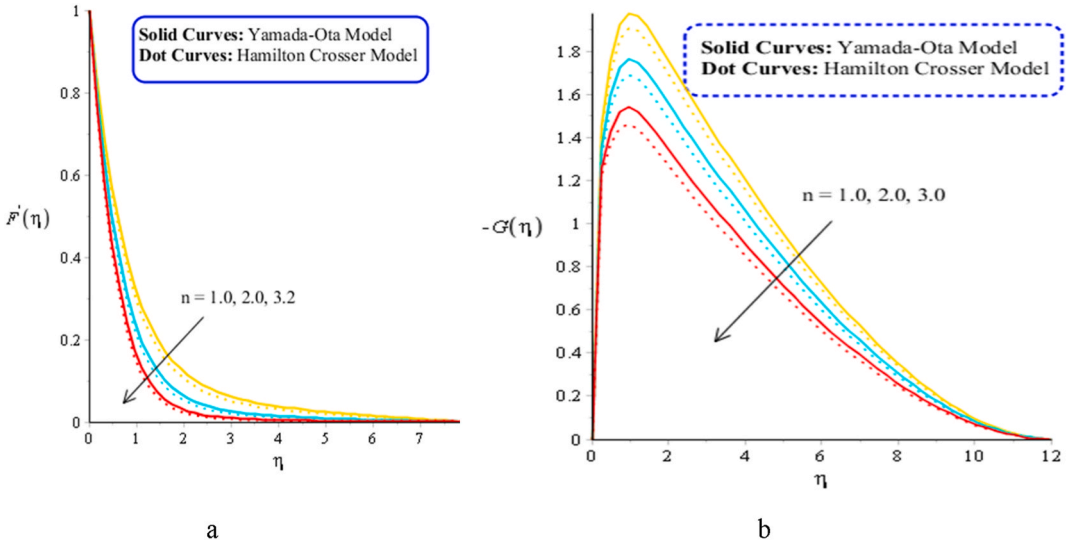

Fig. 5. Different values of n on $F'(\eta)$ and $G(\eta)$ when $M = 0.03, \beta_e = 0.4, \beta_i = 0.2, \Omega = 0.3, \varepsilon_1 = 0.3, Pr = 208, \lambda_a = 0.1, \varphi_1 = 0.004, \varphi_2 = 0.075$.

plotted to notice the variation in thermal thickness when ε_1 is changed. It is noticed that ε_1 has directly proportional relation versus thermal thickness. From this figure, it is noticed that thermal thickness is enhanced when ε_1 is increased. This is because ε_1 has directly proportional relation versus temperature difference. It was addressed that effect of ε_1 is generated using concept of thermal conductivity (variable). Thermal conductivity can be distributed when ε_1 is changed. Alternatively, thermal conductivity is based on ε_1. Moreover, temperature profile for $\varepsilon_1 = 0$ is less than temperature profile for $\varepsilon_1 \neq 0$. Consequently, temperature profile is increased versus enhancement in thermal conductivity. Thermal profile is significantly enhanced versus change in ε_1. Thermal production is enhanced into fluidic particles versus higher impact of time thermal relaxation number (see Fig. 6c). λ_a is occurred using generalized theory. The ability of fluidic particles is enhanced to reestablish thermal energy when λ_a is increased. The parameter regarding λ_a is known as time relaxation number and dimensionless parameter. It is was modeled via non-Fourier's approach. The sortation of thermal energy can be enhanced when λ_a is enhanced. From energy equation, direct proportional investigation has been studied among λ_a and thermal field. Hence, temperature has been magnified versus large values of λ_a. Moreover, it is noticed that thermal production for case of YO-model is higher than thermal production for the case of HC-model.

4.3. Features of wall stresses and thermal wall rate

Table 4 is tabulated to visualize numerical behavior of divergent velocities and Nusselt versus distribution in magnetic number, Hall number and ion slip number. It is concluded that rate flow is inclined when power law number and magnetic parameter are

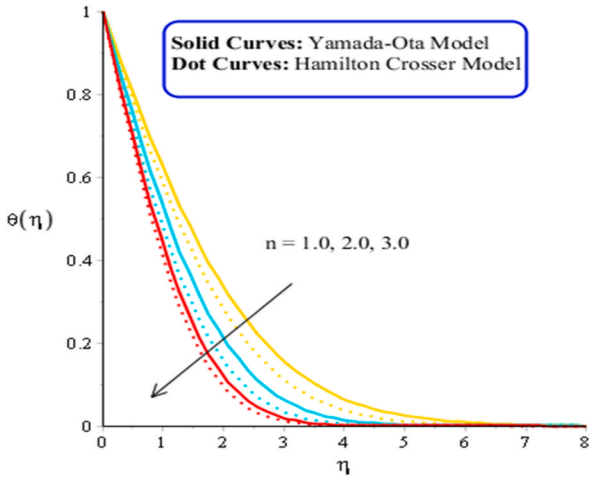

Fig. 6a. Different values of n on $\theta(\eta)$ when $M = 0.07, \beta_e = 0.4, \beta_i = 0.2, \Omega = 0.1, \varepsilon_1 = 0.3, Pr = 206, \lambda_a = 0.8, \varphi_1 = 0.004, \varphi_2 = 0.075$.

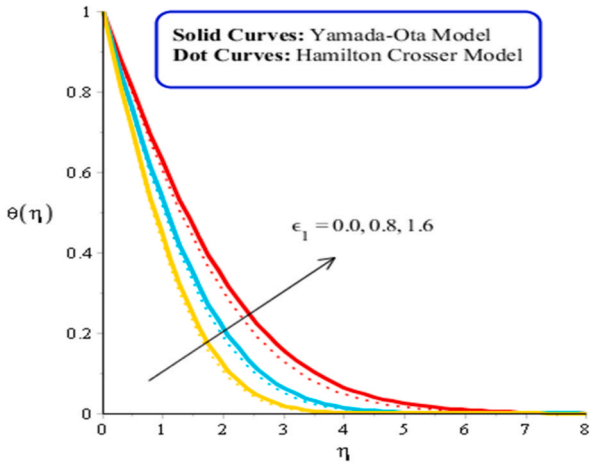

Fig. 6b. Different values of ε_1 on $\theta(\eta)$ when $n = 1, M = 0.003, \beta_e = 0.2, \beta_i = 0.6, \Omega = 0.3, Pr = 206, \lambda_a = 0.1, \varphi_1 = 0.004, \varphi_2 = 0.075$.

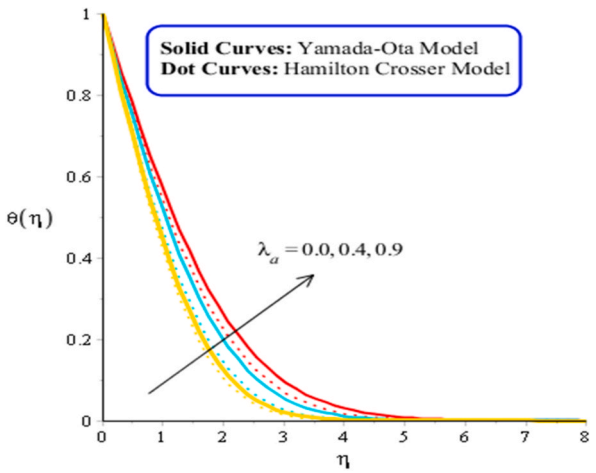

Fig. 6c. Different values of λ_a on $\theta(\eta)$ when $n = 1, M = 0.001, \beta_e = 0.5, \beta_i = 0.2, \Omega = 0.7, \varepsilon_1 = 0.3, Pr = 208, \varphi_1 = 0.004, \varphi_2 = 0.075$.

Table 4
Numerical consequences of several parameters on wall stresses and Nu when $\Omega = 2.5, \varepsilon_1 = 3, Pr = 208, \lambda_a = 2.1, \varphi_1 = 0.004, \varphi_2 = 0.075$.

Variation in parameters		$\frac{1}{(Re)^{\frac{1}{n+1}}} C_f$	$\frac{1}{(Re)^{\frac{1}{n+1}}} C_g$	$\frac{-1}{Nu(Re)^{\frac{1}{n+1}}}$
	0.0	0.5553481139	0.1748620643	0.7829762062
M	0.3	0.5563475983	0.1768582575	0.7839827394
	0.6	0.5583465989	0.1788506305	0.7859957332
	0.0	0.5553024843	0.1746858232	0.7835296293
β_e	0.7	0.5543309637	0.1737491363	0.7841945177
	1.4	0.5533377531	0.1727892774	0.7851092382
	1	0.3516291834	0.08492499066	1.127566389
n	2	0.3950262851	0.1236426023	1.146765643
	3	0.4160832704	0.1352999372	1.289131115
	0.0	0.4161269876	0.1348837811	0.9894678573
β_i	0.6	0.4131312671	0.1330288588	0.9895370946
	1.2	0.4121238814	0.1311215646	0.9896847536

increased. But thermal wall rate declines when magnetic number is inclined. Hall parameter brings declination when Hall number is inclined. Additionally, generalized Ohm's law is observed to be useful to bring enhancement into heat energy. Thermal production for the case of YO-model is higher than thermal production for the case of HC-model. Comparative phenomena among model-I (YO-hybrid nanofluid model) and model-II (Hamilton Crosser hybrid model) with variation in Pr, ε_1 and n on Nusselt number is addressed by Fig. 7a, b and 7c. It is investigated maximum performance of thermally process is gained when Pr and n are enhanced. But opposite trend has been observed against change in ε_1. In additionally, thermally enhancement has been achieved maximum for model-II rather than thermally enhancement for model-I. Hence, it was experienced that model-I is most significant to gain heat transfer rate as compared to heat transfer rate associated with model-I.

5. Conclusions

Three dimensional and rotational flow in power law model for steady flow is considered on a rotating surface. Thermal features are analyzed employing applications of Cattaneo-Christov model. Comparative simulations among model-I and model-II on temperature profile and velocity field within different parameters. Such complex analysis is numerically tackled by finite element approach. Main findings of development are listed below.

- ➢ Velocity fields (in y- and x-directions) increase with enhancement in Hall currents and ion slip while width and thickness decline for momentum layers within enhancement in Hall currents and ion slip;
- ➢ Convergence of developed model was ensured with finite element method;
- ➢ If power law index and radial parameter are higher than zero, then velocity fields (for both directions) decline;
- ➢ By increasing time relaxation, power law index and small parameters, temperature and thermal thickness for layers are magnified;
- ➢ Temperature gradient enhances against with higher values of Prandtl number, small number and power law index;
- ➢ Temperature gradient for mode-II is greater than model-I involving impacts of Prandtl number, n and Pr;
- ➢ Velocity gradient (skin friction coefficient) declines with inclination in Hall currents, ion slip number but opposite trend was addressed against inclination of Lorentz force and n.

Funding

No funding is available.

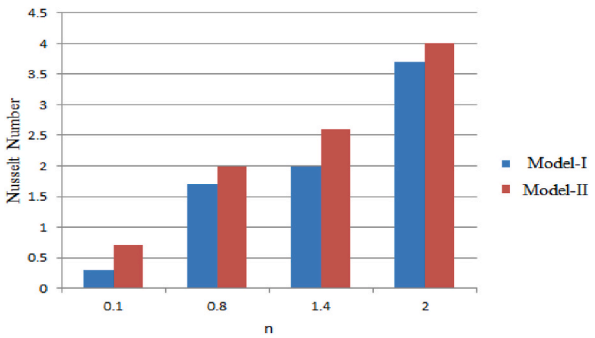

Fig. 7a. Change in Nusselt number with n for model-II and model-I.

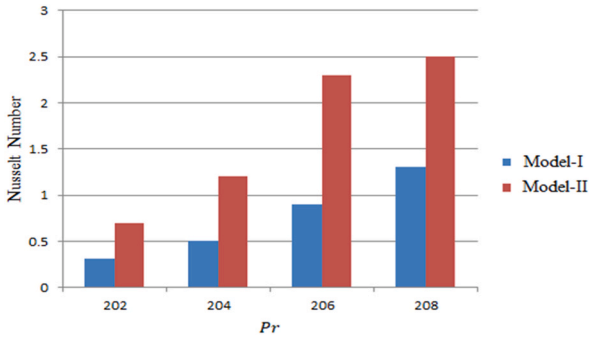

Fig. 7b. Change in Nusselt number with *Pr* for model-II and model-I.

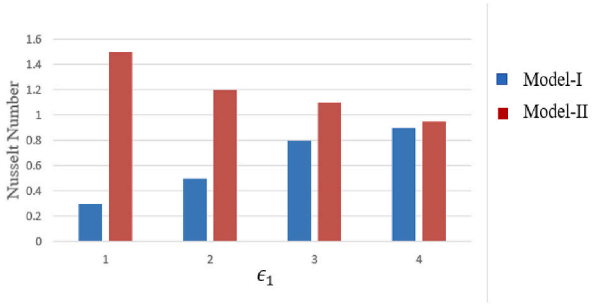

Fig. 7c. Change in Nusselt number with ε_1 for model-II and model-I.

Declaration of competing interest

The authors declare that they have no known competing financial interests or personal relationships that could have appeared to influence the work reported in this paper.

Data availability

Data will be made available on request.

Acknowledgment

This study is supported via funding from Prince Sattam bin Abdulaziz University project number (PSAU/2023/R/1444)

References

[1] U. Nazir, S. Saleem, A. Al-Zubaidi, I. Shahzadi, N. Feroz, Thermal and mass species transportation in tri-hybridized Sisko martial with heat source over vertical heated cylinder, Int. Commun. Heat Mass Tran. 134 (2022), 106003.
[2] M. Sohail, U. Nazir, O. Bazighifan, R.A. El-Nabulsi, M.M. Selim, H. Alrabaiah, P. Thounthong, Significant involvement of double diffusion theories on viscoelastic fluid comprising variable thermophysical properties, Micromachines 12 (8) (2021) 951.
[3] U. Nazir, M. Sohail, U. Ali, E.S.M. Sherif, C. Park, J.R. Lee, M.M. Selim, P. Thounthong, Applications of Cattaneo–Christov fluxes on modelling the boundary value problem of Prandtl fluid comprising variable properties, Sci. Rep. 11 (1) (2021) 1–13.
[4] U. Nazir, M. Sohail, M.B. Hafeez, M. Krawczuk, S. Askar, S. Wasif, An inclination in thermal energy using nanoparticles with casson liquid past an expanding porous surface, Energies 14 (21) (2021) 7328.
[5] M. Sohail, Y.M. Chu, E.R. El-Zahar, U. Nazir, T. Naseem, Contribution of joule heating and viscous dissipation on three-dimensional flow of Casson model comprising temperature dependent conductance utilizing shooting method, Phys. Scripta 96 (8) (2021), 085208.
[6] H. Waqas, S.U. Khan, M. Hassan, M.M. Bhatti, M. Imran, Analysis on the bioconvection flow of modified second-grade nanofluid containing gyrotactic microorganisms and nanoparticles, J. Mol. Liq. 291 (2019), 111231.
[7] U. Nazir, S. Saleem, A. Al-Zubaidi, I. Shahzadi, N. Feroz, Thermal and mass species transportation in tri-hybridized Sisko martial with heat source over vertical heated cylinder, Int. Commun. Heat Mass Tran. 134 (2022), 106003.
[8] Ebrahem A. Algehyne, Essam R. El-Zahar, Muhammad Sohail, Umar Nazir, Hussein AZ. Al-bonsrulah, Dhinakaran Veeman, Bassem F. Felemban, Fahad M. Alharbi, Thermal improvement in pseudo-plastic material using ternary hybrid nanoparticles via Non-Fourier's law over porous heated surface, Energies 14 (23) (2021) 8115.
[9] Muhammad Bilal Hafeez, Wojciech Sumelka, Umar Nazir, Hijaz Ahmad, Sameh Askar, Mechanism of solute and thermal characteristics in a casson hybrid nanofluid based with ethylene glycol influenced by Soret and Dufour effects, Energies 14 (20) (2021) 6818.
[10] F. Mabood, T.A. Yusuf, G. Bognár, Features of entropy optimization on MHD couple stress nanofluid slip flow with melting heat transfer and nonlinear thermal radiation, Sci. Rep. 10 (1) (2020 Nov 5) 1–3.
[11] F. Mabood, T.A. Yusuf, A.M. Rashad, W.A. Khan, H.A. Nabwey, Effects of combined heat and mass transfer on entropy generation due to MHD nanofluid flow over a rotating frame, CMC-COMPUTERS MATERIALS & CONTINUA 66 (1) (2021) 575–587.

[12] A. Ayub, S.Z.H. Shah, Z. Sabir, N.S. Rao, R. Sadat, M.R. Ali, Spectral Relaxation Approach and Velocity Slip Stagnation Point Flow of Inclined Magnetized Cross-Nanofluid with a Quadratic Multiple Regression Model, Waves in Random and Complex Media, 2022, pp. 1–25.
[13] S.L. Shah, A. Ayub, S. Dehraj, H.A. Wahab, K.M. Sagayam, M.R. Ali, R. Sadat, Z. Sabir, Magnetic Dipole Aspect of Binary Chemical Reactive Cross Nanofluid and Heat Transport over Composite Cylindrical Panels, Waves in Random and Complex Media, 2022, pp. 1–24.
[14] Y. Ezaier, A. Hader, A. Latif, L. Amallah, I. Achik, Y. Boughaleb, Morphological properties of the interfaces growth of composite membranes, Mater. Today Proc. (2022).
[15] Y. Ezaier, A. Hader, A. Latif, R. Et Touizi, A. Wakif, Y. Boughaleb, D. Saifaoui, Significance of Deposition and Diffusion Retention on the Performance of the Composite Membrane, Waves in Random and Complex Media, 2022, pp. 1–14.
[16] N.H. Hamad, A. Wakif, A. Alshehri, Towards the dynamics of a radiative-reactive magnetized viscoelastic nanofluid involving gyrotactic microorganisms and flowing over a vertical stretching sheet under multiple convective and stratification constraints, Waves Random Complex Media (2022) 1–31.
[17] E.A. Algehyne, A. Wakif, G. Rasool, A. Saeed, Z. Ghouli, Significance of Darcy-Forchheimer and Lorentz Forces on Radiative Alumina-Water Nanofluid Flows over a Slippery Curved Geometry under Multiple Convective Constraints: a Renovated Buongiorno's Model with Validated Thermophysical Correlations, Waves in Random and Complex Media, 2022, pp. 1–30.
[18] G. Rasool, N.A. Shah, E.R. El-Zahar, A. Wakif, Numerical Investigation of EMHD Nanofluid Flows over a Convectively Heated Riga Pattern Positioned Horizontally in a Darcy-Forchheimer Porous Medium: Application of Passive Control Strategy and Generalized Transfer Laws, Waves in Random and Complex Media, 2022, pp. 1–20.
[19] A. Wakif, M. Zaydan, A.S. Alshomrani, T. Muhammad, R. Sehaqui, New insights into the dynamics of alumina-(60% ethylene glycol+ 40% water) over an isothermal stretching sheet using a renovated Buongiorno's approach: a numerical GDQLLM analysis, Int. Commun. Heat Mass Tran. 133 (2022), 105937.
[20] N.A. Shah, A. Wakif, E.R. El-Zahar, S. Ahmad, S.J. Yook, Numerical Simulation of a Thermally Enhanced EMHD Flow of a Heterogeneous Micropolar Mixture Comprising (60%)-ethylene Glycol (EG),(40%)-water (W), and Copper Oxide Nanomaterials (CuO), Case Studies in Thermal Engineering, 2022, 102046.
[21] M.U. Ashraf, M. Qasim, A. Wakif, M.I. Afridi, I.L. Animasaun, A generalized differential quadrature algorithm for simulating magnetohydrodynamic peristaltic flow of blood-based nanofluid containing magnetite nanoparticles: a physiological application, Numer. Methods Part. Differ. Equ. 38 (3) (2022) 666–692.
[22] M.U. Ashraf, M. Qasim, A. Wakif, M.I. Afridi, I.L. Animasaun, A generalized differential quadrature algorithm for simulating magnetohydrodynamic peristaltic flow of blood-based nanofluid containing magnetite nanoparticles: a physiological application, Numer. Methods Part. Differ. Equ. 38 (3) (2022) 666–692.
[23] A. Wakif, A. Chamkha, I.L. Animasaun, M. Zaydan, H. Waqas, R. Sehaqui, Novel physical insights into the thermodynamic irreversibilities within dissipative EMHD fluid flows past over a moving horizontal riga plate in the coexistence of wall suction and joule heating effects: a comprehensive numerical investigation, Arabian J. Sci. Eng. 45 (11) (2020) 9423–9438.
[24] M. Zaydan, A. Wakif, I.L. Animasaun, U. Khan, D. Baleanu, R. Sehaqui, Significances of blowing and suction processes on the occurrence of thermo-magneto-convection phenomenon in a narrow nanofluidic medium: a revised Buongiorno's nanofluid model, Case Stud. Therm. Eng. 22 (2020), 100726.
[25] G. Rasool, A. Wakif, Numerical spectral examination of EMHD mixed convective flow of second-grade nanofluid towards a vertical Riga plate using an advanced version of the revised Buongiorno's nanofluid model, J. Therm. Anal. Calorim. 143 (3) (2021) 2379–2393.
[26] A. Wakif, I.L. Animasaun, U. Khan, N.A. Shah, T. Thumma, Dynamics of radiative-reactive Walters-b fluid due to mixed convection conveying gyrotactic microorganisms, tiny particles experience haphazard motion, thermo-migration, and Lorentz force, Phys. Scripta 96 (12) (2021), 125239.
[27] M. Alghamdi, A. Wakif, T. Thumma, U. Khan, D. Baleanu, G. Rasool, Significance of variability in magnetic field strength and heat source on the radiative-convective motion of sodium alginate-based nanofluid within a Darcy-Brinkman porous structure bounded vertically by an irregular slender surface, Case Stud. Therm. Eng. 28 (2021), 101428.
[28] M. Zaydan, N.H. Hamad, A. Wakif, A. Dawar, R. Sehaqui, Generalized differential quadrature analysis of electro-magneto-hydrodynamic dissipative flows over a heated Riga plate in the presence of a space-dependent heat source: the case for strong suction effect, Heat Transfer 51 (2) (2022) 2063–2078.
[29] N.K. Reddy, H.A. Swamy, M. Sankar, Buoyant convective flow of different hybrid nanoliquids in a non-uniformly heated annulus, Eur. Phys. J. Spec. Top. 230 (5) (2021) 1213–1225.
[30] M. Sankar, H.K. Swamy, Y. Do, S. Altmeyer, Thermal effects of nonuniform heating in a nanofluid-filled annulus: buoyant transport versus entropy generation, Heat Transfer 51 (1) (2022) 1062–1091.
[31] H. Balasundaram, S. Sathyamoorthi, U. Fernandez-Gamiz, S. Noeiaghdam, S.S. Santra, Hydrocephalic cerebrospinal fluid flowing rotationally with pulsatile boundaries: a mathematical simulation of the thermodynamical approach, Theor. Appl. Mech. Lett. (2022 Dec 8), 100418.
[32] G. Dharmaiah, S. Dinarvand, P. Durgaprasad, S. Noeiaghdam, Arrhenius activation energy of tangent hyperbolic nanofluid over a cone with radiation absorption, Results Eng. 16 (2022), 100745.
[33] N. Vedavathi, G. Dharmaiah, S. Noeiaghdam, U. Fernandez-Gamiz, A chemical engineering application on hyperbolic tangent flow examination about sphere with Brownian motion and thermo phoresis effects using BVP5C, Case Stud. Therm. Eng. 40 (2022), 102491.
[34] Z. Zamm, A. Vcr, Three-dimensional flow of a power-law fluid due to a stretching flat surface, ZAMM, Z. angew. Math Mech 75 (5) (1995) 3x9–394.
[35] M.A. Sadiq, Non fourier heat transfer enhancement in power law fluid with mono and hybrid nanoparticles, Sci. Rep. 11 (1) (2021) 1–14.
[36] M. Sohail, U. Nazir, S. Naz, A. Singh, K. Mukdasai, M.R. Ali, M.J. Khan, A.M. Galal, Utilization of Galerkin finite element strategy to investigate comparison performance among two hybrid nanofluid models, Sci. Rep. 12 (1) (2022) 1–15.
[37] N. Vedavathi, G. Dharmaiah, S. Noeiaghdam, U. Fernandez-Gamiz, A chemical engineering application on hyperbolic tangent flow examination about sphere with Brownian motion and thermo phoresis effects using BVP5C, Case Stud. Therm. Eng. 40 (2022), 102491.
[38] N. Hameed, S. Noeiaghdam, W. Khan, B. Pimpunchat, U. Fernandez-Gamiz, M.S. Khan, A. Rehman, Analytical analysis of the magnetic field, heat generation and absorption, viscous dissipation on couple stress casson hybrid nano fluid over a nonlinear stretching surface, Results Eng. 16 (2022), 100601.
[39] Y.M. Chu, A. Abbasi, K. Al-Khaled, W. Farooq, S.U. Khan, M.I. Khan, S.M. Eldin, K. Guedri, Mathematical Modeling and Computational Outcomes for the Thermal Oblique Stagnation Point Investigation for Non-uniform Heat Source and Nonlinear Chemical Reactive Flow of Maxwell Nanofluid, Case Studies in Thermal Engineering, 2022, 102626.
[40] S. Dero, T.N. Abdelhameed, K. Al-Khaled, L.A. Lund, S.U. Khan, I. Tlili, Contribution of suction phenomenon and thermal slip effects for radiated hybrid nanoparticles (Al_2O_3-Cu/H_2O) with stability framework, Int. J. Mod. Phys. B (2022), 2350147.